ADVANCED FUNCTIONAL MATERIALS

FULL PAPER

DOI: 10.1002/adfm.200500816

Structural and Electrostatic Complexity at a Pentacene/Insulator Interface**

By *Kanan Puntambekar*, *Jinping Dong*, *Greg Haugstad*, and *C. Daniel Frisbie**

The properties of organic-semiconductor/insulator (O/I) interfaces are critically important to the operation of organic thin-film transistors (OTFTs) currently being developed for printed flexible electronics. Here we report striking observations of structural defects and correlated electrostatic-potential variations at the interface between the benchmark organic semiconductor pentacene and a common insulator, silicon dioxide. Using an unconventional mode of lateral force microscopy, we generate high-contrast images of the grain-boundary (GB) network in the first pentacene monolayer. Concurrent imaging by Kelvin probe force microscopy reveals localized surface-potential wells at the GBs, indicating that GBs will serve as charge-carrier (hole) traps. Scanning probe microscopy and chemical etching also demonstrate that slightly thicker pentacene films have domains with high line-dislocation densities. These domains produce significant changes in surface potential across the film. The correlation of structural and electrostatic complexity at O/I interfaces has important implications for understanding electrical transport in OTFTs and for defining strategies to improve device performance.

1. Introduction

The advancement of organic electronics for applications in solar-energy conversion, printed circuitry, displays, and solid-state lighting depends upon the optimization of a variety of organic-semiconductor interfaces.[1,2] Organic-semiconductor/insulator (O/I) interfaces,[3] in particular, are critical to the operation of organic thin-film transistors (OTFTs) currently being developed for printed flexible electronics.[4–6] In an OTFT, the presence or absence of gate-induced charge at the O/I interface determines whether the OTFT is ON (current flows) or OFF (no current flows). Structural and electrostatic disorder in the first few layers of the organic semiconductor next to the insulator (i.e., in the O/I interfacial region) lowers the OTFT ON current, reduces the switching speed, and can increase the threshold voltage, all of which are undesirable. Minimizing disorder at O/I interfaces is therefore essential for improving device performance. Unfortunately, rational approaches are hampered by limited understanding of both interfacial structure and the correlation of structure with electrical properties.

Here we report scanning probe microscopy (SPM) observations of polycrystalline microstructure and defects in 2–5 nm thick interfacial layers of the benchmark organic semiconductor pentacene ($C_{22}H_{14}$) grown on the insulator silicon dioxide. We demonstrate that grain boundaries (GBs) and high line-dislocation densities produce striking and unexpected variations in the surface electrostatic potential of the interfacial pentacene layers on SiO_2. The surface-potential distributions of O/I interfaces are critically important to OTFT operation,[7] as discussed below. Correlations between structure and surface potential therefore have significant implications for electrical-transport models and for understanding structure–property relationships in OTFTs. Visualization of rich structural and electrostatic complexity at crystalline O/I interfaces also opens future opportunities for rational efforts to tailor the properties of these interfaces by physical or chemical means.

2. Results and Discussion

Our investigation focuses on the pentacene/SiO_2 interface, which is widely employed in OTFTs[8–10] because of the favorable electrical-transport characteristics of pentacene (including a high field-effect hole mobility of approximately 1 $cm^2 V^{-1} s^{-1}$) and the convenience of fabricating high-quality amorphous SiO_2 insulating layers. Pentacene on SiO_2 exhibits Stranski–Krastanov growth, where coalescence of the first polycrystalline monolayer (ML) is followed by defect-assisted stacking of subsequent MLs in overlying islands.[11] The molecules stand vertically or near vertically in each layer (d_{001} = 1.54–1.61 nm), and pack in a herringbone, edge-to-face packing motif in-

[*] Prof. C. D. Frisbie, Dr. K. Puntambekar
Department of Chemical Engineering and Materials Science
University of Minnesota
421 Washington Ave. SE, Minneapolis, MN 55455 (USA)
E-mail: frisbie@cems.umn.edu
Dr. J. Dong, Dr. G. Haugstad
Characterization Facility, Institute of Technology
University of Minnesota
100 Union St. SE, Minneapolis, MN 55455 (USA)

[**] This work was partially supported by the NSF Materials Research Science and Engineering Center program (DMR# 0212302). K. P. gratefully acknowledges support from a University of Minnesota Doctoral Dissertation Fellowship. The authors thank J. Pflaum, Universität Stuttgart, for suggesting the chemical etching method in ref. [27]. Supporting Information is available online from Wiley InterScience or from the author.

 © 2006 WILEY-VCH Verlag GmbH & Co. KGaA, Weinheim WILEY InterScience DISCOVER SOMETHING GREAT

plane.[12,13] The early stages of pentacene-film growth on amorphous SiO_2 have been investigated by SPM,[11] photoelectron-emission microscopy (PEEM),[14] and grazing-incidence X-ray diffraction (GIXD).[12,15,16] The grain structure of a complete pentacene ML has, however, not been imaged previously. The structure of this layer is critically important because it is the layer in which most of the gate charge resides during OTFT operation.

We have discovered that an unconventional mode of lateral force microscopy (LFM),[17,18] which we term transverse shear microscopy (TSM), produces high-contrast images of the grain structure in coalesced pentacene MLs. Figure 1A shows a contact-mode topography image of a pentacene film consisting of a coalesced first ML with some nucleated dendritic islands of the second ML. This image was obtained by measuring the vertical deflection of the SPM cantilever as it scanned over the surface of the sample (i.e., in constant-force mode). The grains in the first ML are not evident in this topographic map. However, for a scan direction (***S***) parallel to the long axis of the tip cantilever (Fig. 1D), we also tracked the "transverse shear force" or twisting of the cantilever due to the lateral force acting perpendicular to the scan vector. The resulting transverse shear images (Figs. 1B–C) show remarkable contrast between the randomly oriented grains, which is not evident in corresponding topography images.

We postulate that the transverse shear results from the interaction of the tip with two dissimilar sets of molecules in the *ab* plane labeled with red and blue circles (Fig. 1E); the two sets of molecules have different orientation vectors (**1** and **2** in Fig. 1E). If the scan vector (***S***) of the cantilever is along the crystallographic *a*- or *b*-direction, then the angle between **1** and ***S*** is the same as the angle between **2** and ***S***, resulting in no net transverse shear. If the tip is scanned along any other direction, then there is a net transverse shear component on the cantilever that is equal and opposite during the trace and retrace scans (Figs. 1B and C). This effect is maximized when ***S*** is along the diagonal <110> directions of a pentacene crystallite. For example, for grain "G1", the brightest contrast in the trace image (Fig. 1B) and darkest contrast in the retrace image (Fig. 1C) implies that the [110] direction of grain "G1" is oriented along ***S***. The opposite sense of contrast for grain "G2" indicates a relative orientation of nearly 90° between the two grains. To confirm this mechanism, the sample was systematically rotated (Fig. 1F) and the trace-minus-retrace shear signal over a few grains (inset of Fig. 1F) was recorded. The plot in Figure 1F shows an approximately 180° periodicity, as predicted based on the two-dimensional herringbone packing of the pentacene crystal structure.

Therefore, as originally described by Last and Ward,[17] image contrast in the transverse shear method reflects crystallographic direction. The transverse shear images in Figures 1B and C not only visualize the network of faceted pentacene grains in the coalesced ML, but also elucidate the relative orientation of the grains.

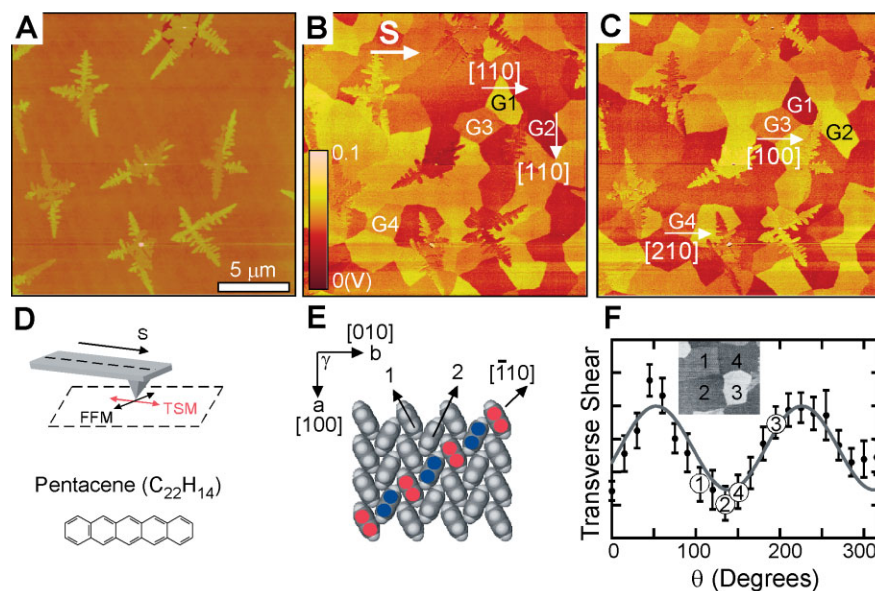

Figure 1. Polycrystalline microstructure of a coalesced pentacene monolayer. Contact-mode atomic force microscopy (AFM) topography (A) and transverse shear trace (B) and retrace (C) images of a vapor-deposited pentacene ML on SiO_2. The scheme in (D) defines the scan direction vector, ***S***, which, during transverse shear imaging, is parallel to the long axis of the cantilever (FFM: friction force microscopy). The herringbone molecular packing in the pentacene monolayer (E) with $a = 5.912$ Å, $b = 7.556$ Å, and $\gamma = 90.0°$ [12]. Transverse shear contrast is maximized for ***S*** aligned along the diagonal <110> directions and is minimized for ***S*** aligned along the *a*- or *b*-directions. The plot (F) demonstrates the variation of the transverse shear contrast (trace–retrace) with sample rotation angle (i.e., grain orientation) for the four grains shown in the inset. The ~180° periodicity of the contrast reflects the symmetry of the pentacene unit cell and confirms the sensitivity of TSM to grain orientation. Selected grains G1–G4 in (B) and (C) are labeled with their corresponding crystallographic orientations determined by analysis of the transverse shear contrast.

Our central result is the observation of significant variations in surface potential at the pentacene/SiO_2 interface and the correlation of the surface potential with specific structural features. The surface potential is the electrostatic potential energy of a surface-confined (or interface-confined) charge, and is determined by crystal structure, electronic energy levels, and the presence of defects, dipoles, fixed charges, contaminants, and applied electric fields. Variations in surface potential of the O/I interface in an OTFT will affect the threshold voltage and the spatial distribution of gate-induced charge. Peaks and troughs in the surface potential can also serve as barriers or traps for charge transported parallel to the O/I interface, thereby lowering the ON current in a transistor. Thus, there is a direct connection between the O/I surface potential and OTFT performance.

Figure 2A shows a transverse shear image of several grains in a pentacene ML, where the topography (not shown) is featureless. Using Kelvin probe force microscopy (KFM)[19,20] in air, we have

© 2006 WILEY-VCH Verlag GmbH & Co. KGaA, Weinheim

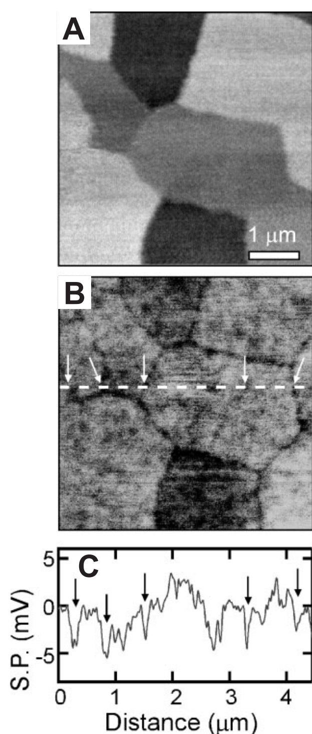

Figure 2. Transverse shear (A) and surface potential (B) maps of a small region of a pentacene ML on SiO_2, showing potential wells at the GBs. The corresponding topography image (not shown) is featureless. C) Surface-potential (SP) line section corresponding to the dashed line in (B). The arrows indicate the GB potential wells. The measured depth of the wells averages between ~–5 and –10 mV over several samples.

mapped the surface potential of the same region. The surface potential map in Figure 2B clearly shows the presence of negative potentials at the GBs. Line scans, as shown in Figure 2C, indicate that the GB potential wells are approximately –5 to –10 mV in depth and 50–100 nm in width, although these numbers are likely to be larger and smaller, respectively, because of the limited spatial resolution of the measurement.[21] The origin of the GB potential is presently not clear. Whereas in conventional semiconductors GB potentials can arise because of trapped charge, here the mechanism could also involve selective oxygen or water adsorption at the GBs or simply structural disorder.[22,23]

The importance of GBs in electrical transport in OTFTs is still being debated.[10,24,25] The small magnitude of the measured GB potential compared to the thermal energy ($k_BT = 25$ meV; T: temperature; k_B: the Boltzmann constant) at room temperature indicates that the GBs will serve as shallow hole traps. We also observe that surface-potential variations within the grains are comparable to the drops at the GBs (Figs. 2B and C), making it ambiguous whether the GBs are the principal bottlenecks to hole transport. Nevertheless, Figure 2B provides direct evidence that GB potentials can exist in polycrystalline organic-semiconductor films. Further quantitative KFM imaging in combination with transport measurements on small numbers of grains can determine the extent to which small GB potentials affect charge transport.

KFM and conventional friction imaging[18] of multilayered pentacene films on SiO_2 reveal even greater electrostatic and structural inhomogeneity. Figure 3 shows topography (Fig. 3A) and corresponding surface-potential (Fig. 3B) and conventional friction (Fig. 3C) images of a 2–3 ML (3–5 nm) thick pentacene film on SiO_2. Examination of Figures 3B and C shows that there is substantial contrast in both images, and that the surface-potential and friction maps have discrete contrast levels, not a continuous grayscale (Figs. 3D–F and Supporting Information, Fig. S2).

Comparison of the topography (Figs. 3A and D) and the surface-potential data (Figs. 3B and D, and Supporting Information, Fig. S2) reveals that changes in surface potential occur in discrete steps corresponding to the number of stacked pentacene MLs. The step in surface potential between the SiO_2 and 1 ML thick pentacene layer is ~+150 mV, and the average step between 1 and 2 MLs is ~+50 mV (Fig. 3E and Supporting Information, Fig. S2). The surface-potential difference between successive MLs decreases with increasing ML number and is <15 mV by the fourth ML (Fig. 3E and Supporting Information, Fig. S4B). Previous qualitative imaging by PEEM of multilayer pentacene films on SiO_2 has also revealed the presence of surface-potential steps associated with discrete pentacene layers, but quantitative measurement of the surface-potential differences was not reported.[14] The contrast we observe in air between the first ML and SiO_2 is qualitatively similar to the +500 mV contrast measured by Chen et al. for isolated pentacene ML islands on SiO_2 in vacuum.[26] The surface-potential contrast between the pentacene layers may result from screening of a dipole that originates from the difference in work function between pentacene and SiO_2.[26] We observe an opposite sign of the surface potential for an n-type organic semiconductor grown on SiO_2 (Supporting Information, Fig. S1B), supporting the view that the interface dipole arises in part from intrinsic work-function differences between the semiconductor and the insulator.

Importantly, we observe unexpected surface-potential contrast within the second ML (Fig. 3B). Two distinct surface-potential domains with a difference of 25 ± 5 mV are evident (2A, B in Fig. 3B). There is also a one-to-one correlation between domains of high (more positive) surface potential and domains of low friction in the second ML (Figs. 3B and C), suggesting that the underlying causes for the surface potential and friction contrast are related. The friction contrast is greater than 2:1 between domains 2A and 2B in the second ML (Fig. 3F), indicating that there are significant differences in structure that are not detectable in the topography image.

We hypothesized that the friction contrast between domains 2A and 2B was due to different defect densities. In order to visualize defects, we etched the pentacene multilayer films in sulfuric acid solution.[27] Chemical etching is frequently used to reveal microstructure and defects in polycrystalline metals and ceramics,[28] and has also been employed to reveal dislocations in organic single crystals.[27] For immersion times of ~5–10 s, we found that the etching was limited to the low-surface-potential, high-friction domains in the second ML (2A). Figure 4 shows topographic and LFM images of an etched sample. Par-

 © 2006 WILEY-VCH Verlag GmbH & Co. KGaA, Weinheim

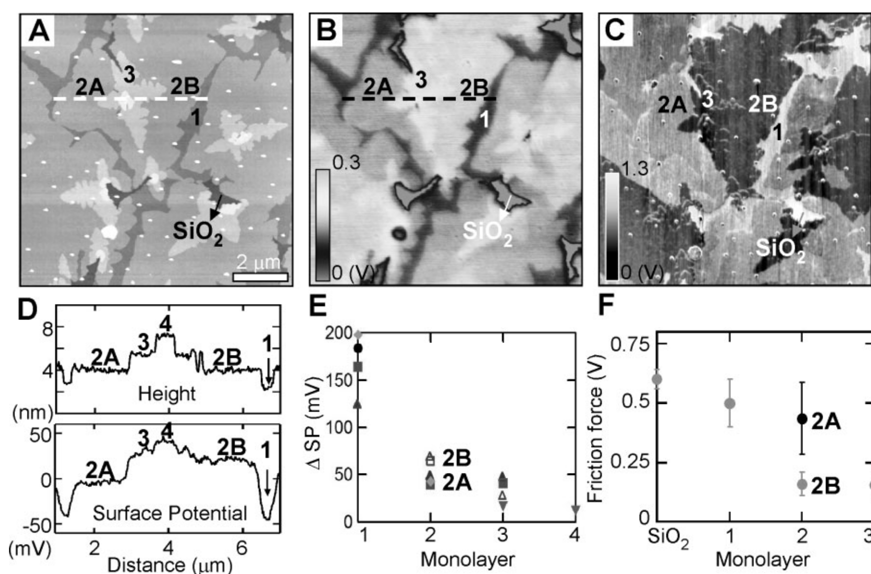

Figure 3. Structural and electrostatic inhomogeneity in pentacene multilayers. Topography (A), surface-potential (B), and conventional friction (C) maps of the same region of a 3–5 nm thick pentacene multilayer film on SiO_2. Regions 1, 2, and 3 correspond to 1, 2, and 3 ML thick films; 2A and 2B are distinct domains within the second ML. Line sections (D) show height and surface-potential variations across regions 1, 2A, 2B, and 3, with steps in surface potential generally corresponding to the number of stacked MLs. Importantly, regions 2A and B within the second ML have no difference in height but show clear surface-potential and friction contrast. Comparison of (B) and (C) reveals a one-to-one correspondence between the SP and friction contrast for regions 2A and 2B. The 2A domain has a lower surface potential and higher friction; domain 2B has higher surface potential and lower friction. From the line sections (D), the height for each monolayer is 1.53 ± 0.3 nm. The plot (E) demonstrates that the magnitude of the surface-potential steps (ΔSP) between successive MLs decreases as the number of MLs increases. ΔSP of monolayer 1 indicates the surface-potential difference between the first ML and the SiO_2 substrate. Different symbols correspond to different samples or regions on the same sample. The friction force decreases as the number of MLs increases (F). The SiO_2 substrate displays the highest friction. The friction difference is large (> 2:1) between regions 2A and 2B in the second ML.

allel grooves are visible in two distinct high-friction domains, indicating the presence of line dislocations aligned along a specific crystallographic direction. Shorter etches reveal grooves developing from a series of aligned pinholes that nucleate along the dislocation (Supporting Information, Fig. S3).

Previous imaging studies by transmission electron microscopy[23,29] and scanning tunneling microscopy[30] have demonstrated the presence of line dislocations in pentacene crystals and films, and X-ray scattering has been used to infer the presence of dislocations in pentacene.[15] Direct visualization of the distribution of dislocations at device-relevant O/I interfaces has, however, not been reported.

Our images indicate that the line dislocations are confined only to the high-friction, low-surface-potential domains of the second ML. We do not observe dislocations in the first or third ML. It is likely that stress build-up, localized in the second ML because of epitaxial or orientational mismatch with respect to the first ML, is the cause of the dislocations. It is also probable that the high density of line dislocations in local domains of the second ML leads to both a different local surface potential[31] and a higher dissipative interaction with the tip, resulting in higher friction contrast.[32]

We also observe that the unaffected regions of the high-friction domains (region 2A) of the second ML in Figure 4B show similar contrast to the low-friction domains (region 2B). It is likely that the chemical etching of the line dislocations relieves the stress build-up in the high-friction domains, thus resulting in a lower-friction contrast. A shorter etch, as shown in Fig. S3, still shows a discernable contrast between regions 2A and 2B, while for slightly longer etches, this contrast is nearly absent (Fig. 4B).

The fact that the dislocations are parallel in a given domain indicates that there is a single common Burgers vector. We propose two possible dislocation models. In the first, shown in Figure 4C, the etched parallel grooves derive from an edge dislocation along <110> with a corresponding Burgers vector, $\boldsymbol{b} = 1/2\langle 1\bar{1}0\rangle$. We assign the Burgers vector based on the fact that the diagonal <110> directions have the highest linear molecular density (resulting in the smallest possible Burgers vector). There are two principal <110> diagonal directions, oriented at 76° with respect to each other, that must be differentiated in order to rationalize the observation of parallel dislocations. One plausible explanation is that the stress state in a given domain will favor one dislocation direction over another. Others have reported that the two diagonal directions in pentacene are actually slightly inequivalent.[12,33,34] However, it is likely that the structure of ultrathin pentacene films, which is different from that of bulk pentacene,[12] will have to be determined in detail before clear conclusions can be drawn regarding an inherent preference for a given dislocation direction.

Our second model (Fig. 4D) proposes that the Burgers vector has both in-plane (along $\langle 1\bar{1}0\rangle$) and out-of-plane (along [001]) components. Motivation for this model is the observation of buckling of pentacene films by scanning tunneling microscopy[35] and reports by others that a principal slip direction in oligoacene crystals lies along [001].[15,23] We note that out-of-plane displacements of pentacene molecules in the second ML may be responsible for the nucleation of screw dislocations along [001] that are known to facilitate the rapid growth of thicker pentacene films.[15] Thus, the proposed out-of-plane component of the line dislocations in the second ML may ultimately be responsible for driving the dislocation-assisted vertical growth of pentacene films.

The observation of structural defects and correlated surface-potential domains in ultrathin pentacene layers at the SiO_2 interface has important implications for electrical transport. In a pentacene OTFT, the majority of the gate-induced holes

© 2006 WILEY-VCH Verlag GmbH & Co. KGaA, Weinheim

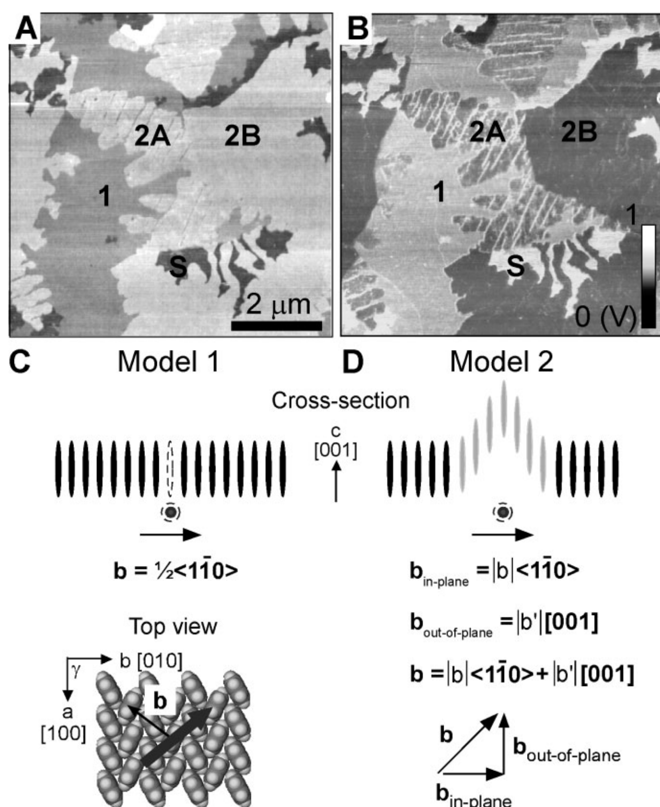

Figure 4. Exposure of line dislocations by chemical etching. After a ~5 s exposure to sulfuric acid, topography (A) and friction (B) images reveal etched parallel grooves in the second ML due to the presence of line dislocations. The line dislocations are localized in the high-friction (2A) regions in the second ML. The short etch does not detectably affect the exposed first ML of the sample (region 1), nor does it affect the low-friction regions of the second ML (2B) and the regions with thicknesses greater than 3 MLs (Fig. S3). S indicates the SiO_2 substrate. The fact that the dislocations are parallel in a given domain indicates a common Burgers vector, ***b***. (C) and (D) show two models for the dislocations. In the first model (C), the dislocation line lies along <110>, with ***b*** along <1$\bar{1}$0>. These directions are shown schematically in edge-on and top-down views of the *ab* plane. The missing line of pentacene molecules is indicated by the dashed oval, and the dislocation direction is indicated by the heavy arrow in the *ab* plane. In the second model (D), the dislocation line is a local buckling of the second ML along <110> due to out-of-plane sliding of pentacene molecules, resulting in a Burgers vector with both in-plane and out-of-plane components, $\boldsymbol{b} = |b|\langle 1\bar{1}0\rangle + |b'|[001]$.

reside within a few nanometers of the O/I interface, and the presence of inter- and intralayer surface-potential differences will affect the spatial distribution and transport of holes. For example, the lateral intralayer heterogeneity in the surface potential will mean that holes are distributed inhomogeneously in the conducting channel of a transistor and will be concentrated in the lower potential domains. Likewise, the interlayer surface-potential differences will tend to further confine the holes to the lower-potential first ML of pentacene. Hole transport will also be affected because GBs and line dislocations may serve as traps that will lower the hole mobility.[36] Importantly, we note that the surface-potential steps we measure are remarkably similar to the activation energies reported for field-effect hole mobilities in pentacene OTFTs,[9,10] suggesting that the cause of activated transport is the heterogeneity that we observe in the surface electrostatic potential.

3. Conclusion

We have demonstrated a direct correlation between structural and electrostatic disorder at an important O/I interface widely employed in organic electronics. Similar results for other organic-semiconductor/insulator combinations indicate that our observations are of general importance for crystalline O/I interfaces (Supporting Information, Figs. S1 and S5). In light of the robust connection between surface potential and OTFT operation, these results provide conclusive evidence that structural and electrostatic complexity of O/I interfaces must be accounted for in the physical description of organic field-effect transport. Additionally, the microscopy techniques demonstrated here should facilitate improvements in the electrical performance of O/I interfaces by furnishing a strategy for direct assessment of materials-design efforts aimed at decreasing defect densities and surface-potential variations.

4. Experimental

Sample Preparation: All the samples were prepared by thermal evaporation of pentacene onto amorphous silicon dioxide films (300 nm thick) thermally grown on p-doped silicon wafers. Parameters for pentacene vapor deposition on silicon dioxide: Deposition rate: 0.01 to 0.02 Å s^{-1}; substrate temperature: 50 °C; chamber vacuum ~4×10^{-7} Torr (1 Torr ≈ 133 Pa).

Scanning Probe Microscopy/Atomic Force Microscopy: All measurements were performed using a Veeco Metrology (previously Digital Instruments) Nanoscope III A multimode atomic force microscope under atmospheric conditions.

Kelvin Probe Force Microscopy/Scanning Surface Potential Microscopy: KFM is a noncontact technique in which the local variations in the surface potential of a sample are mapped in conjunction with topography, enabling a direct correlation between the two [19,37]. The characterization was done using the surface-potential mapping mode of the atomic force microscope with probe tips fabricated by Mikromasch USA (NSC35-B tips, Ti/Pt coated, resonant frequency 240–405 kHz, lift height 10–15 nm). In KFM, the surface potential is measured using a nulling technique with the help of a feedback circuit [19,20]. The surface potential is measured in a dual-scan mode in which the tip is lifted off the surface by a few nanometers and retraces the topography scan. Spatial resolution of the method is affected by tip/cantilever geometry, lift height during the surface-potential scan, and surface contamination. In addition, the tip measures a weighted average of surface potential around each point [21,37,38]. As a result, the actual potential drop at the GB in Figure 2B will be higher than the number extracted from the image.

Friction Force Microscopy and Transverse Shear Microscopy: FFM, or conventional LFM, is a contact-mode technique, where the local variations in the sliding friction between the tip and the sample can be mapped in conjunction with topography, enabling a direct correlation between the two [18]. FFM was done using tips fabricated by Veeco Metrology, USA (Triangular silicon nitride contact mode tips, model DNP, force constant: 0.06–0.58 N m^{-1}). The fast-scan direction of the tip was perpendicular to the long axis of the cantilever such that frictional force on the tip exerted a torque about the cantilever's principal axis, measured via the horizontal difference signal of the quadrant photodetector (Fig. 1D).

© 2006 WILEY-VCH Verlag GmbH & Co. KGaA, Weinheim

All the FFM images shown in the main figures (Figs. 3 and 4) are the trace scans. The plot in Figure 3F is obtained from the difference image (trace minus retrace). The raw data were measured in volts using analysis software (SPM analysis, copyright 2005, Greg Haugstad). Friction contrast measured using FFM has been shown previously to be sensitive to local disorder [32,39,40]. We note that sample rotation did not change the intralayer friction contrast in the second pentacene ML, indicating that the contrast is not dominated by friction anisotropy.

Transverse shear microscopy (TSM) [17] is a marked variation of conventional LFM. While simultaneously recording contact-mode topography, we tracked the twisting of the cantilever due to lateral force acting *perpendicular* to the scan vector (Fig. 1D). The grain specificity in TSM results from an anisotropic transverse shear stress field in different crystalline domains.

Sample Registration: In order to find the same area for both KFM and LFM imaging, we evaporated a patterned gold film on some regions of the sample (> 100 μm away from the region of interest) as an alignment marker.

Etching Procedure: The etching medium used was a 1:2 solution of sulfuric acid (96 %) in deionized water (volume fraction). The etch was followed by thorough rinsing with water and nitrogen blow drying [27].

Received: November 16, 2005
Final version: December 20, 2005
Published online: March 23, 2006

[1] W. Y. Gao, A. Kahn, *J. Phys. Condens. Matter* **2003**, *15*, S2757.
[2] H. Ishii, K. Sugiyama, E. Ito, K. Seki, *Adv. Mater.* **1999**, *11*, 605.
[3] J. Veres, S. Ogier, G. Lloyd, D. de Leeuw, *Chem. Mater.* **2004**, *16*, 4543.
[4] J. A. Rogers, Z. Bao, H. E. Katz, A. Dodabalapur, *Thin-Film Transistors*, Marcel Dekker, New York **2003**, p. 377.
[5] C. D. Dimitrakopoulos, P. R. L. Malenfant, *Adv. Mater.* **2002**, *14*, 99.
[6] H. Sirringhaus, T. Kawase, R. H. Friend, T. Shimoda, M. Inbasekaran, W. Wu, E. P. Woo, *Science* **2000**, *290*, 2123.
[7] L. Burgi, H. Sirringhaus, R. H. Friend, *Appl. Phys. Lett.* **2002**, *80*, 2913.
[8] H. Klauk, T. N. Jackson, *Solid State Technol.* **2000**, *43*, 63.
[9] P. V. Pesavento, R. J. Chesterfield, C. R. Newman, C. D. Frisbie, *J. Appl. Phys.* **2004**, *96*, 7312.
[10] D. Knipp, R. A. Street, A. R. Volkel, *Appl. Phys. Lett.* **2003**, *82*, 3907.
[11] R. Ruiz, D. Choudhary, B. Nickel, T. Toccoli, K. C. Chang, A. C. Mayer, P. Clancy, J. M. Blakely, R. L. Headrick, S. Iannotta, G. G. Malliaras, *Chem. Mater.* **2004**, *16*, 4497.
[12] S. E. Fritz, S. M. Martin, C. D. Frisbie, M. D. Ward, M. F. Toney, *J. Am. Chem. Soc.* **2004**, *126*, 4084.
[13] C. C. Mattheus, A. B. Dros, J. Baas, G. T. Oostergetel, A. Meetsma, J. L. de Boer, T. T. M. Palstra, *Synth. Met.* **2003**, *138*, 475.
[14] F. J. Meyer zu Heringdorf, M. C. Reuter, R. M. Tromp, *Nature* **2001**, *412*, 517.
[15] B. Nickel, R. Barabash, R. Ruiz, N. Koch, A. Kahn, L. C. Feldman, R. F. Haglund, G. Scoles, *Phys. Rev. B* **2004**, *70*, 125 401.
[16] H. C. Yang, T. J. Shin, M. M. Ling, K. Cho, C. Y. Ryu, Z. N. Bao, *J. Am. Chem. Soc.* **2005**, *127*, 11 542.
[17] J. A. Last, M. D. Ward, *Adv. Mater.* **1996**, *8*, 730.
[18] R. W. Carpick, M. Salmeron, *Chem. Rev.* **1997**, *97*, 1163.
[19] M. Nonnenmacher, M. P. O'Boyle, H. K. Wickramasinghe, *Appl. Phys. Lett.* **1991**, *58*, 2921.
[20] M. Fujihira, *Annu. Rev. Mater. Sci.* **1999**, *29*, 353.
[21] H. O. Jacobs, P. Leuchtmann, O. J. Homan, A. Stemmer, *J. Appl. Phys.* **1998**, *84*, 1168.
[22] J. E. Northrup, M. L. Chabinyc, *Phys. Rev. B* **2003**, *68*, 041 202(R).
[23] L. F. Drummy, C. Kubel, D. Lee, A. White, D. C. Martin, *Adv. Mater.* **2002**, *14*, 54.
[24] E. M. Muller, J. A. Marohn, *Adv. Mater.* **2005**, *17*, 1410.
[25] G. Horowitz, M. E. Hajlaoui, *Adv. Mater.* **2000**, *12*, 1046.
[26] L. W. Chen, R. Ludeke, X. D. Cui, A. G. Schrott, C. R. Kagan, L. E. Brus, *J. Phys. Chem. B* **2005**, *109*, 1834.
[27] N. T. Corke, A. A. Kawada, J. N. Sherwood, *Nature* **1967**, *213*, 62.
[28] G. Dieter, *Mechanical Metallurgy*, McGraw Hill, New York **1986**.
[29] M. Brinkmann, S. Graff, C. Straupe, J.-C. Wittmann, C. Chaumont, F. Nuesch, A. Aziz, M. Schaer, L. J. Zuppiroli, *J. Phys. Chem. B* **2003**, *107*, 10 531.
[30] D. Fichou, F. Charra, A. O. Gusev, *Adv. Mater.* **2001**, *13*, 555.
[31] B. S. Simpkins, E. T. Yu, P. Waltereit, J. S. Speck, *J. Appl. Phys.* **2003**, *94*, 1448.
[32] R. W. Carpick, Q. Dai, D. F. Ogletree, M. Salmeron, *Tribol. Lett.* **1998**, *5*, 91.
[33] J. Cornil, J. P. Calbert, J. L. Brédas, *J. Am. Chem. Soc.* **2001**, *123*, 1250.
[34] J. E. Northrup, M. L. Tiago, S. G. Louie, *Phys. Rev. B* **2002**, *66*, 121 404.
[35] J. H. Kang, D. da Silva, J. L. Brédas, X. Y. Zhu, *Appl. Phys. Lett.* **2005**, *86*, 152 115.
[36] S. Hayashi, I. Okada, N. Ide, K. Kojima, *J. Phys. Condens. Matter* **1992**, *4*, L379.
[37] H. O. Jacobs, H. F. Knapp, S. Mueller, A. Stemmer, *Ultramicroscopy* **1997**, *69*, 39.
[38] H. O. Jacobs, H. F. Knapp, S. Mueller, A. Stemmer, *Rev. Sci. Instrum.* **1999**, *70*, 1756.
[39] G. Haugstad, J. A. Hammerschmidt, W. L. Gladfelter, in *Interfacial Properties on the Submicron Scale* (Eds: J. Frommer, R. M. Overney), ACS Books, Washington, DC **2001**, p. 230.
[40] X. D. Xiao, J. Hu, D. H. Charych, M. Salmeron, *Langmuir* **1996**, *12*, 235.

© 2006 WILEY-VCH Verlag GmbH & Co. KGaA, Weinheim